

## Article

# Study on the Performance of Active Embedded Steel Wire Knot Form in Silicone Graphene Composite Thermal Insulation Structure Integrated System

Xiaoxia Zhao <sup>1</sup>, Dajiang Geng <sup>1,\*</sup>, Zhiqiang Cheng <sup>2</sup> , Zhicheng Bai <sup>1</sup>, Mingjian Long <sup>1</sup>, Yang Chen <sup>1</sup>, Qingqing Lu <sup>3</sup> and Wei Ying <sup>4</sup>

<sup>1</sup> China Construction 4th Engineering Bureau 6th Co., Ltd., Shanghai 201100, China

<sup>2</sup> Shanghai Road and Bridge (Group) Co., Ltd., Shanghai 201100, China

<sup>3</sup> Shanghai Engineering Research Center of Green Pavement Materials, Shanghai 201100, China

<sup>4</sup> China Resources Power Hubei Co., Ltd., Chibi 437300, China

\* Correspondence: gdj1410704@alumni.tongji.edu.cn; Tel.: +86-15026400259

**Abstract:** Based on the advantages of the silicone graphene composite thermal insulation board, it was used to replace traditional plywood in the external wall formwork system, and the active embedded steel wire knot form in silicone graphene composite thermal insulation structure integrated system was designed. Firstly, the theoretical model of steel wire drawing resistance was established by theoretical analysis method, and the rationality of the theoretical model was verified by combining relevant experimental data. The relationship between multiple variables and steel wire pull-out resistance was analyzed. Then, combined with the theory of wind pressure strength of the exterior wall of a building structure, the layout form and the corresponding number of embedded steel wires of thermal insulation board under different building heights were analyzed. Finally, the silicone graphene composite thermal insulation board and ordinary plywood were compared and analyzed from the force of perspective of external wall formwork. The results showed that the pull-out resistance of steel wire was directly proportional to the diameter of steel wire, embedded depth, and embedded deflection angle. With the increase of building height, the number of steel wires to be arranged also increased. When the thickness of the silicone graphene composite thermal insulation board is not less than 80 mm, the anti-deformation effect is close to that of the ordinary plywood, which can meet the construction requirements of the external wall formwork. It can ensure the energy conservation and thermal insulation of the external wall, integrate the building's exterior wall and thermal insulation structure of the building, and achieve the purpose of exemption from formwork removal.

**Keywords:** thermal insulation structure integration; embedded steel wire knot; pull-out resistance; wind pressure strength; free from formwork removal; silicone graphene composite board



**Citation:** Zhao, X.; Geng, D.; Cheng, Z.; Bai, Z.; Long, M.; Chen, Y.; Lu, Q.; Ying, W. Study on the Performance of Active Embedded Steel Wire Knot Form in Silicone Graphene Composite Thermal Insulation Structure Integrated System.

*Buildings* **2023**, *13*, 705. <https://doi.org/10.3390/buildings13030705>

Academic Editor: Ahmed Senouci

Received: 16 February 2023

Revised: 28 February 2023

Accepted: 6 March 2023

Published: 7 March 2023



**Copyright:** © 2023 by the authors. Licensee MDPI, Basel, Switzerland. This article is an open access article distributed under the terms and conditions of the Creative Commons Attribution (CC BY) license (<https://creativecommons.org/licenses/by/4.0/>).

## 1. Introduction

The energy consumption of the construction industry accounts for one-third of total energy consumption, and the greenhouse gas emissions of the construction industry account for two-thirds of global greenhouse gas emissions. In recent years, population growth and the transformation of human lifestyle have further increased the greenhouse gas emissions of the construction industry, thus affecting environmental, social, and economic development [1]. Therefore, reducing building energy consumption and carbon dioxide emissions is crucial for sustainable development. In the construction industry, the enclosure structure is regarded as a critical factor in improving building energy efficiency. Thermal insulation materials are often used in buildings to reduce heat transfer and meet heating and cooling requirements, thus improving indoor temperature comfort. Proper

thermal insulation materials can reduce noise and fire risk, achieve indoor and outdoor energy balance, and reduce greenhouse gas emissions [2].

According to the summary of existing relevant research results, building insulation materials can be roughly divided into traditional, advanced, and recyclable types. Traditional thermal insulation materials mainly include glass wool [3,4], rock wool [3,4], slag wool [3], expanded polystyrene [3,4], extruded polystyrene [3], polyurethane [5], foam glass [6,7], and perlite [8]. Examples of advanced thermal insulation materials include aerogel [9,10], vacuum insulation board [11,12], nano insulation material [13], hollow panel [14], reflective foam [15], plant fiber [16], and biological fiber [17]. Recyclable thermal insulation materials mainly include granular rubber [18], cork waste [18], textile waste [19], polystyrene fiber [20], and glass fiber [21], among others.

At present, most of the research focuses on the relevant performance parameters of thermal insulation materials, including thermal conductivity [22], energy storage [23], moisture absorption [24], fire prevention [24], noise reduction [25], and so on. There are few practical engineering applications. Mohammad [26] summarized the application of glass fiber, rock wool, polyethylene, polyurethane, perlite, and other thermal insulation materials in building exterior walls and roofs. Zhao [27] introduced the aluminum alloy thermal insulation integrated decorative panel, which is directly fixed on the exterior wall of the building in combination with the keel and anchor bolt and can realize the thermal insulation decoration function of the exterior wall of the building. In recent years, based on the development requirements of ultra-low energy consumption in the construction industry, the integration technology of thermal insulation and structure can ensure the long-term stability and low energy consumption of the external wall thermal insulation system, which has become one of the necessary options for energy conservation and thermal insulation in current construction projects. Li et al. [28] studied the mechanical properties of the glass bead form-free shear wall based on the indoor shear span ratio test, which provides a basis for the practical application of the project. Li et al. [29] designed a reinforced rock wool composite insulation board to achieve the effect of thermal insulation and structural integration. In Shanghai, a new type of silicone graphene composite thermal insulation board has been widely used in the structural system of construction engineering without formwork removal due to its good safety, durability, and weather resistance, and its internal coating of galvanized steel wire mesh has sufficient strength.

From the perspective of construction technology, the traditional thermal insulation structure lays the thermal insulation layer on the outer wall after completing the cast-in-place concrete curing. Unfortunately, the cross-construction is complicated, slow, difficult to coordinate, and has potential quality and safety hazards. The integrated technology of thermal insulation structure optimizes the construction process. It improves construction efficiency by using the composite thermal insulation board as the outer formwork of the wall and enhancing the bonding strength between the thermal insulation board and the wall through special passive anchors. However, the existing integrated technology of thermal insulation structure requires the addition of passive anchors for connection. When the anchors are embedded, it is easy to cause brittle damage and risk slurry leakage of the insulation board. The number and location of anchors restrict the bond strength between the insulation board and the structural layer, increase the risk of hollowing out, and increase the cost of auxiliary materials.

Considering the good thermal insulation performance of the silicone graphene material [30–34], in order to solve the problems existing in the above-integrated system of thermal insulation structure, this paper proposes adding steel wires in the silicone graphene composite board, changing the passive anchoring to an active tie, actively enhancing the bonding strength of the insulation layer and the concrete base layer through the tie steel wire, ensuring full adhesion without cavities, and reducing the cost of auxiliary materials and operating procedures. The arrangement of tie steel wires determines the overall bonding effect between the silicone graphene composite board and structure. In this paper, by establishing the theoretical model of steel wire pull-out and the theoretical calculation

of steel wire wind-resistant pressure, the relationship between the pull-out force of steel wire and the diameter of steel wire, the density of matrix concrete, the embedded depth of steel wire and the deflection angle of steel wire is determined. It further determines the arrangement form and quantity of steel wire corresponding to different building heights. By analyzing and comparing the bending strength and deflection deformation of the thermal insulation board and the traditional plywood formwork, it is evident that the silicone graphene composite board can be used in the external wall formwork system to replace the traditional plywood. This can ensure the energy conservation and thermal insulation of the external wall, integrate the external wall and thermal insulation structure of the building, and achieve the purpose of avoiding the removal of the formwork.

## 2. Calculation of Uplift Force of Steel Wire Embedded Integrated Board

### 2.1. Theoretical Model of Steel Wire Pull-out Resistance

In order to establish the pull-out model of steel wire in a concrete matrix, as shown in Figure 1, the following assumptions are made:

- (1) Both steel wire and concrete matrix are elastic materials.
- (2) When the steel wire is embedded into the concrete matrix, a pull-out zone is formed between the steel wire and the matrix. The contact friction between the steel wire and the matrix, the mechanical bite force when the matrix shrinks, and so on, together constitute the interface bonding strength of the two media.
- (3) Under the action of external forces, the pull-out effect of steel wire and concrete can be divided into debonding stage and the pull-out stage [30].

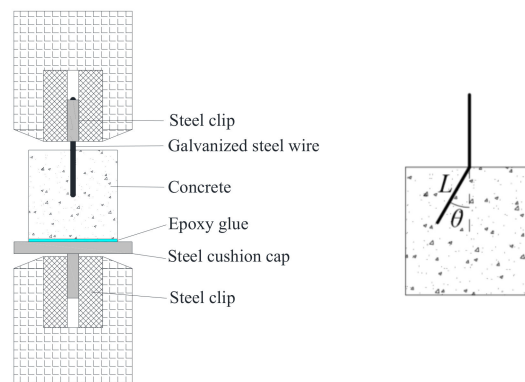


**Figure 1.** Schematic diagram of steel wire pull-out test [35].

According to the above assumptions, there is interfacial bonding strength  $f$  between steel wire and concrete matrix, the relationship between interfacial bond strength  $f$  and the pull-out displacement of steel wire  $\delta$  can be expressed as [36]:

$$f = \begin{cases} f_0, & \delta \leq \delta_0 \\ f_0 + f(\delta), & \delta > \delta_0 \end{cases} \quad (1)$$

where  $f_0$  is the peak bond strength at the debonding stage;  $f(\delta)$  is the attenuation function of contact interface bond strength;  $\delta$  is the steel wire pull-out displacement;  $\delta_0$  is the corresponding pull-out displacement at the end of the debonding stage.

When the steel wire is debonded, the interfacial bond strength decreases rapidly. This paper mainly analyzes the maximum pull-out force of the steel wire. Considering the displacement of debonding stage where  $\delta_0$  is negligible compared with the length  $L$  of steel wire embedded in the concrete matrix, the maximum pull-out resistance of steel wire can be expressed as [35]:

$$F_{\max}(d, f_0, L) = f_0 \pi d L + F_0 \quad (2)$$

where  $d$  is the diameter of steel wire,  $L$  is the embedded depth of steel wire, and  $F_0$  is the elastic bonding force between steel wire and concrete matrix [37].

When the embedded direction of the steel wire deflects from the concrete matrix, the maximum pull-out force of the steel wire can be expressed as:

$$F_{\max}(d, f_0, L, \theta) = F_{\max}(d, f_0, L, 0) \cdot e^{\varepsilon \cdot \theta} \quad (3)$$

where  $\theta$  is the embedded deflection angle of steel wire,  $\varepsilon$  is the deflection angle influence coefficient, taken as  $\varepsilon = 0.5$  [38].

Refer to relevant test data [30,34] to establish the peak bond strength  $f_0$  and concrete density  $\rho$  Fitting relationship between:

$$f_0(\rho) = a \cdot \rho - b \quad (4)$$

where,  $a$  and  $b$  are fitting parameters.

In addition, it can be found [35,39] that when the density of the concrete matrix is large enough, the elastic bond force  $F_0$  between steel wire and concrete matrix presents a convergence trend, and when the density of concrete  $\rho = 1000 \text{ kg/m}^3$  and above,  $F_0 = 200 \text{ N}$ . The expression of the maximum pull-out force of steel wire can be obtained from the Equation (2) to Equation (4):

$$F_{\max}(d, \rho, L, \theta) = [200 + \pi d \cdot f_0(\rho) \cdot L] \cdot e^{\varepsilon \cdot \theta} \quad (5)$$

## 2.2. Verification of Theoretical Model of Steel Wire Pull-Out Resistance

From the above Equation (5), it can be seen that the maximum tensile strength of steel wire is related to the diameter of steel wire  $d$ , the embedded depth of steel wire  $L$ , and the density of concrete matrix  $\rho$  (corresponding strength grade), steel wire embedded deflection angle  $\theta$  of select  $d = 2 \text{ mm}$  hot-dip galvanized steel wire with the tensile strength of 17 kN, taking into account 28 d curing age of concrete matrix and concrete density  $\rho = 2385 \text{ kg/m}^3$  (C30), respectively for steel wire embedding depth  $L$  and steel wire embedding deflection angle  $\theta$  perform validation [35,39]. The specific test process used the single factor variable method to study the influence of the concrete density  $\rho$ , the embedded depth of steel wire  $L$  and the steel wire embedded deflection angle  $\theta$  on the maximum pull-out force  $F_{\max}$  of the steel wire. The concrete density is  $500 \text{ kg/m}^3$ ,  $700 \text{ kg/m}^3$ ,  $1000 \text{ kg/m}^3$  and  $2385 \text{ kg/m}^3$ , respectively. When the embedded deflection angle of the steel wire is  $0^\circ$  and  $45^\circ$ , the embedded depth is 20 mm, 30 mm, 40 mm, 50 mm, 60 mm, 70 mm, 80 mm, 90 mm and 100 mm, respectively. When the embedded depth of the steel wire is 50 mm, the embedded deflection angle is  $0^\circ$ ,  $10^\circ$ ,  $20^\circ$ ,  $30^\circ$ ,  $40^\circ$  and  $45^\circ$ , respectively. From Figures 2–4, it can be seen that the relation Equation (5) of the maximum pull-out force of steel wire can better verify the relevant test data. When test result data is substituted into Equation (4), results are  $a = 1.42 \times 10^3 \text{ N}\cdot\text{m/kg}$ ;  $b = 4.00 \times 10^5 \text{ Pa}$ ;  $R^2 = 0.96$ .

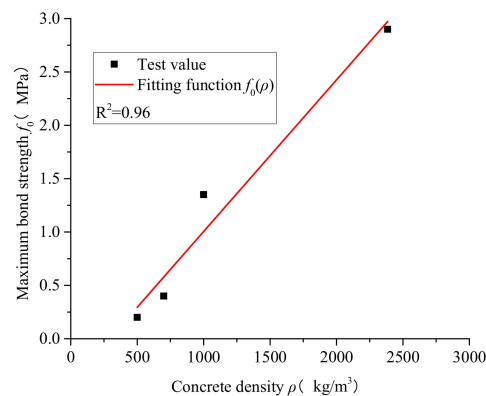
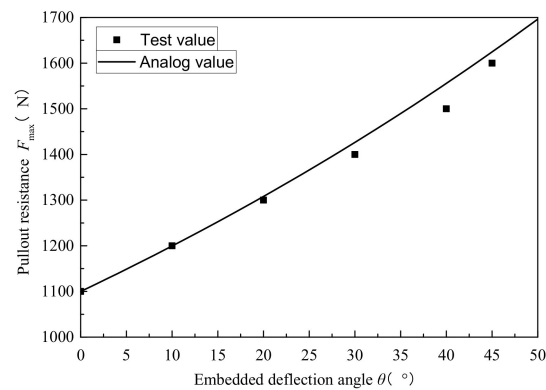
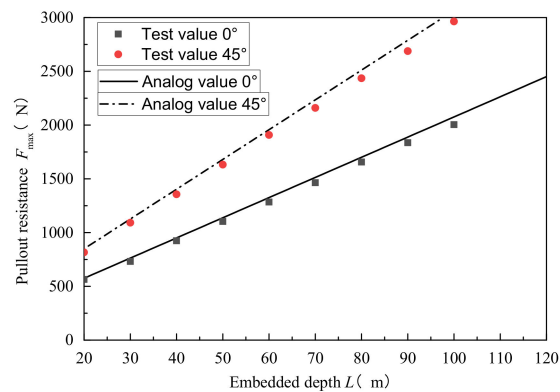


Figure 2. Relationship between concrete density and bond strength of steel wire.



**Figure 3.** Influence of deflection angle of embedded steel wire on tensile force ( $L = 50$  mm).



**Figure 4.** Influence of depth of embedded steel wire on tensile force.

### 2.3. Wind Pressure Resistance Strength of the Integrated Thermal Insulation Structure System

The wind pressure resistance strength of the integrated thermal insulation structure system shall comply with the following provisions [40]:

$$R_K \geq K \cdot W_K \quad (6)$$

where  $W_K$  is the standard value of wind load ( $\text{kN/m}^2$ );  $K$  is the wind load resistance safety factor of the integrated thermal insulation structure system,  $K = 3.3$  [40].

$$R_K = F_{\max} \cdot n \cdot \eta \quad (7)$$

where  $n$  is the number of steel wires per square meter;  $F_{\max}$  is the maximum pull-out force of the steel wire;  $\eta$  is the reduction factor,  $\eta = 0.5$ .

Wind load strength calculation [41]:

$$W_K = \beta_z \cdot \mu_s \cdot \mu_z \cdot \omega_0 \quad (8)$$

where  $\beta_z$  is the gust coefficient at height  $z$ ;  $\mu_s$  is the local shape coefficient of wind load;  $\mu_z$  is the wind pressure height variation coefficient;  $\omega_0$  is the standard value of basic wind pressure.

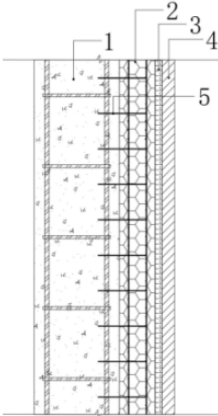
## 3. Wind Pressure Resistance Performance Analysis of Steel Wire Embedded Thermal Insulation and Structural Integration System

### 3.1. Basic Information on Thermal Insulation and Integrated Structural Board

Based on the advantages of a composite thermal insulation board, this paper designs the actively embedded steel wire knot form in a composite thermal insulation structure integrated system. A number of embedded wires and double-layer steel wire mesh are overlapped by spot welding to form an extended steel wire skeleton. The skeleton is placed

inside the thermal insulation material when making the thermal insulation board to form steel wire-embedded composite thermal insulation board. The thermal insulation board can be used as a formwork, free from disassembly, when used for on-site casting/PC prefabrication, and the embedded steel wires mainly play the role of active binding and anchoring. The design structure is shown in Table 1, and the relevant performance parameters of the composite thermal insulation board are shown in Table 2.

**Table 1.** Design and construction of silicone graphene composite thermal insulation structure integrated system.

Base Wall 1	Thermal Insulation Layer 2	Plastering Layer 3	Finish Layer 4	Tie Steel Wire 5	Structural Diagram
Cast-in-situ/ prefabricated wall	Composite thermal insulation board	Plastering mortar (built-in alkali resistant glass fiber mesh)	External wall flexible putty + adhesive + face brick	Double-layer galvanized steel wire mesh + tie steel wire	

**Table 2.** Relevant performance parameters of silicone graphene composite thermal insulation board.

Test Indicators	Performance Requirements	Test Results	Test Method Basis
Dry density ( $\text{kg}/\text{m}^3$ )	150–300	184	GB/T 5486-2008 [42]
Compressive strength (Mpa)	$\geq 0.30$	0.33	GB/T 5486-2008
Tensile strength perpendicular to the plate surface (Mpa)	$\geq 0.20$	0.21	JGJ 144-2019 [43]
Thermal conductivity coefficient, 25 °C ( $\text{W}/\text{m}\cdot\text{K}$ )	$\leq 0.055$	0.050	GB/T 10294-2008 [44]
Bending load (N)	$\geq 3000$	3179	GB/T 19631-2005 [45]
Bending deformation (mm)	$\geq 6$	$\geq 6$	GB/T 8813-2008 [46]
Impact resistance (J)	The first-floor wall of the building and the wall at the door and window positions	10	JGJ 144-2019
	Corresponding walls on the second floor and above	3	JGJ 144-2019
Combustion performance level	A (A2)	—	GB 8624-2012 [47]
Wind pressure resistance value (kPa)	—	10.63	JGJ 144-2019

Combined with the above theoretical model of steel wire pull-out resistance, consider the diameter of steel wire  $d$ , the embedded depth of steel wire  $L$ , the density of matrix concrete  $\rho$  (Corresponding strength grade), and embedded deflection angle of steel wire  $\theta$ . The corresponding values of different factors affecting the pull-out performance of steel wire are shown in Table 3. Based on the wind pressure strength theory of the integrated system of thermal insulation structure, the Shanghai area is taken as an example (the ground roughness is classified as Class C) to analyze the arrangement form and quantity of embedded steel wires of thermal insulation board corresponding to different building heights ( $z$ ). The parameters related to wind load strength are shown in Table 4.

**Table 3.** Different influencing factors and corresponding variables.

Variable	Value
Steel wire diameter $d$ (mm)	1.0, 1.5, 2.0, 3.0, 4.0
Concrete density $\rho$ (kg/m <sup>3</sup> )	2385 (C30), 2390 (C35), 2400 (C40), 2410 (C45), 2420 (C50)
Embedded depth of steel wire $L$ (mm)	30, 40, 50, 60, 80, 100
Embedded deflection angle of steel wire $\theta$ (°) (Tilt Down)	0, 15, 30, 45, 60

**Table 4.** Parameter values related to wind load strength.

Height above Ground $z$ (m)	Gust Coefficient $\beta_z$	Wind Pressure Height Variation Coefficient $\mu_z$	Local Shape Coefficient of Wind Load $\mu_s$	The Standard Value of Basic Wind Pressure $\omega_0$ (kN/m <sup>2</sup> )
10	2.05	0.65		
20	1.99	0.74		
30	1.90	0.88		
40	1.85	1.0		
50	1.81	1.10		
60	1.78	1.20	2.0	0.4
70	1.75	1.28		
80	1.73	1.36		
90	1.71	1.43		
100	1.69	1.50		

### 3.2. Results and Discussion

#### 3.2.1. Analysis of Tensile Strength of Steel Wire

Figure 5 shows the relationship between steel wire diameter  $d$  and pull-out force  $F_{\max}$  ( $L = 50$  mm,  $\theta = 0^\circ$ ). It can be seen from the figure that the corresponding density range of C30~C50 concrete is not apparent (2385 kg/m<sup>3</sup>~2420 kg/m<sup>3</sup>), so the change range of the pull-out force produced by the same steel wire diameter is almost unchanged. However, for the same concrete matrix, the pull-out resistance increases with the increase in wire diameter. This is mainly because the larger the diameter, the larger the contact area between the steel wire and the concrete matrix, resulting in greater maximum pull-out force.

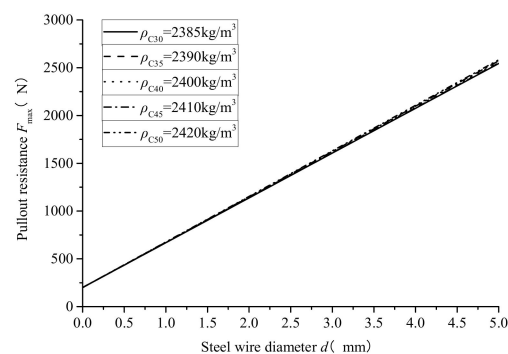
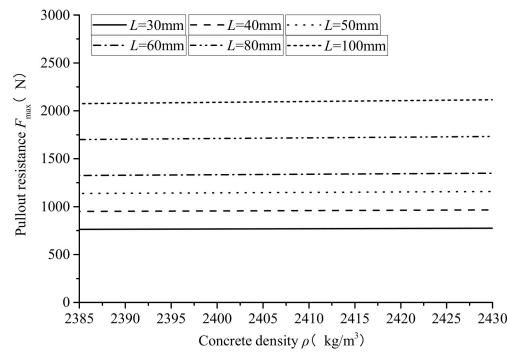
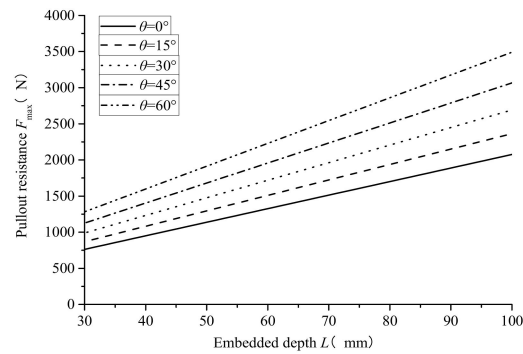
**Figure 5.** Relationship between wire steel diameter and pull-out peak load ( $L = 50$  mm,  $\theta = 0^\circ$ ).

Figure 6 shows the concrete density at different embedded depths of steel wire  $\rho$  relation with uplift force  $F_{\max}$  ( $d = 2$  mm,  $\theta = 0^\circ$ ). It can be seen from the figure that for the same concrete matrix, the pull-out force increases with the increase of the embedded depth of the steel wire, which also reflects that the pull-out force of the steel wire is greatly affected by the interface contact area. However, the increase in concrete density has little effect on the pull-out resistance of steel wire, which further validates the conclusion in Figure 5 above.



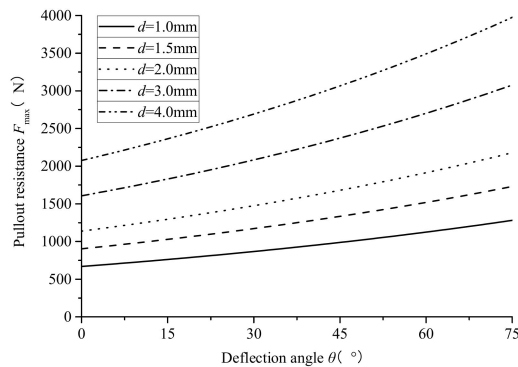
**Figure 6.** Relationship between concrete density and pull-out peak load ( $d = 2 \text{ mm}$ ,  $\theta = 0^\circ$ ).

Figure 7 shows the relationship between the embedded depth  $L$  of the steel wire and the uplift force  $F_{\max}$  ( $d = 2 \text{ mm}$ ,  $\rho = 2385 \text{ kg/m}^3$ ). It can be seen from the figure that the pull-out force of steel wire is significantly affected by the embedded deflection angle, and the pull-out force of steel wire increases with the increase of deflection angle. This result is due to angular deflection of the embedded steel wire, with the drawing direction still perpendicular to the concrete, subjecting the embedded steel wire to contact friction and mechanical bite force in both directions. Therefore, when the embedded steel wire has a certain angle deflection, it will enhance the pull-out resistance of the steel wire.



**Figure 7.** Relationship between embedded depth of steel wire and pull-out peak load ( $d = 2 \text{ mm}$ ,  $\rho = 2385 \text{ kg/m}^3$ ).

Figure 8 shows the embedded deflection angle of steel wire under different diameters of steel wire  $\theta$  relation with uplift force  $F_{\max}$  ( $L = 50 \text{ mm}$ ,  $\rho = 2385 \text{ kg/m}^3$ ). This result further validates the conclusion in Figure 7, and with the synchronous increase of steel wire diameter, the pull-out resistance of the wire will be further enhanced.



**Figure 8.** Relationship between embedded deflection angle of steel wire and pull-out peak load ( $L = 50 \text{ mm}$ ,  $\rho = 2385 \text{ kg/m}^3$ ).

To sum up, it is evident that the pull-out resistance of steel wire is affected by the diameter  $d$  of steel wire, the embedded depth  $L$  of steel wire, and the embedded deflection angle of steel wire  $\theta$ . The impact is large and significant, and the pull-out resistance is proportional to the three factors. On the contrary, when the concrete density (i.e., strength) reaches  $2385 \text{ kg/m}^3$  (C30) and above, the impact on the steel wire's pull-out performance is significant.

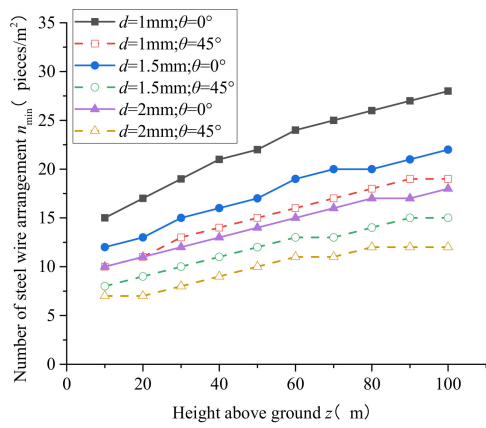
### 3.2.2. Result Analysis of Steel Wire Arrangement

For Shanghai, consider the steel wire diameter  $d = 1 \text{ mm}$ ,  $1.5 \text{ mm}$ ,  $2 \text{ mm}$ , steel wire embedding depth  $L = 30 \text{ mm}$ ,  $40 \text{ mm}$ ,  $50 \text{ mm}$ ,  $60 \text{ mm}$ ,  $80 \text{ mm}$ ,  $100 \text{ mm}$ , and steel wire embedding deflection angle  $\theta = 0^\circ$ ,  $45^\circ$ . The number of steel wires of thermal insulation board corresponding to different ground heights  $z$  of the building is  $n_{\min}$ , and the calculation results are shown in Figure 9. It can be seen from the figure that the number of steel wire arrangements is inversely proportional to the diameter of the steel wire, the embedded depth of the steel wire, and the embedded deflection angle of the steel wire. It has also been observed that the number of steel wires to be arranged increases with the increase in building height. In other words, the arrangement of steel wires determines the bonding performance of the thermal insulation board. When the overall bonding strength meets the requirements of wind pressure resistance, the minimum number of steel wires corresponding to different building heights can be obtained. Therefore, the number of embedded steel wires in the thermal insulation board per unit area depends on the building structure's external wall load and the steel wire's pull-out performance.

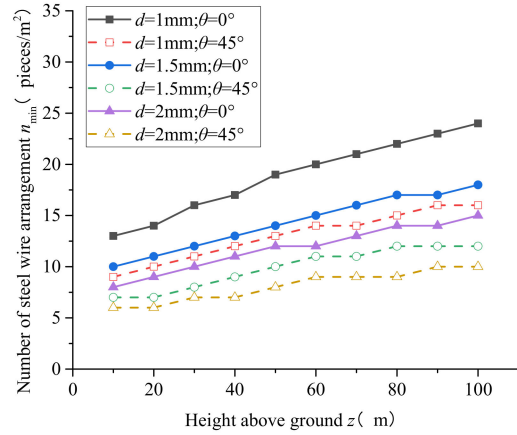
Considering the error in the actual project, in order to ensure the stability of the integrated system of thermal insulation structure, the arrangement quantity of steel wires for the composite thermal insulation board during production is recommended to be  $n_{\min} \times 2$  (unit: pieces/m<sup>2</sup>), as shown in Tables 5 and 6.

**Table 5.** Number of steel wire layouts per square meter of integrated thermal insulation structure system ( $\theta = 0^\circ$ ).

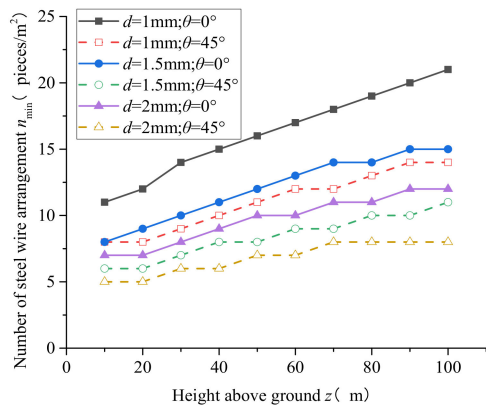
Height above Ground $z$ (m)	$z < 20$	$20 \leq z < 50$	$50 \leq z \leq 100$
$d = 1 \text{ mm}; L = 30 \text{ mm}$	$\geq 34$	$\geq 44$	$\geq 56$
$d = 1.5 \text{ mm}; L = 30 \text{ mm}$	$\geq 26$	$\geq 34$	$\geq 44$
$d = 2 \text{ mm}; L = 30 \text{ mm}$	$\geq 22$	$\geq 28$	$\geq 36$
$d = 1 \text{ mm}; L = 40 \text{ mm}$	$\geq 28$	$\geq 38$	$\geq 48$
$d = 1.5 \text{ mm}; L = 40 \text{ mm}$	$\geq 22$	$\geq 28$	$\geq 36$
$d = 2 \text{ mm}; L = 40 \text{ mm}$	$\geq 18$	$\geq 24$	$\geq 30$
$d = 1 \text{ mm}; L = 50 \text{ mm}$	$\geq 24$	$\geq 32$	$\geq 41$
$d = 1.5 \text{ mm}; L = 50 \text{ mm}$	$\geq 18$	$\geq 24$	$\geq 30$
$d = 2 \text{ mm}; L = 50 \text{ mm}$	$\geq 14$	$\geq 20$	$\geq 24$
$d = 1 \text{ mm}; L = 60 \text{ mm}$	$\geq 22$	$\geq 28$	$\geq 36$
$d = 1.5 \text{ mm}; L = 60 \text{ mm}$	$\geq 16$	$\geq 22$	$\geq 26$
$d = 2 \text{ mm}; L = 60 \text{ mm}$	$\geq 12$	$\geq 16$	$\geq 22$
$d = 1 \text{ mm}; L = 80 \text{ mm}$	$\geq 18$	$\geq 24$	$\geq 30$
$d = 1.5 \text{ mm}; L = 80 \text{ mm}$	$\geq 12$	$\geq 16$	$\geq 22$
$d = 2 \text{ mm}; L = 80 \text{ mm}$	$\geq 10$	$\geq 14$	$\geq 16$
$d = 1 \text{ mm}; L = 100 \text{ mm}$	$\geq 14$	$\geq 20$	$\geq 24$
$d = 1.5 \text{ mm}; L = 100 \text{ mm}$	$\geq 10$	$\geq 14$	$\geq 18$
$d = 2 \text{ mm}; L = 100 \text{ mm}$	$\geq 8$	$\geq 12$	$\geq 14$



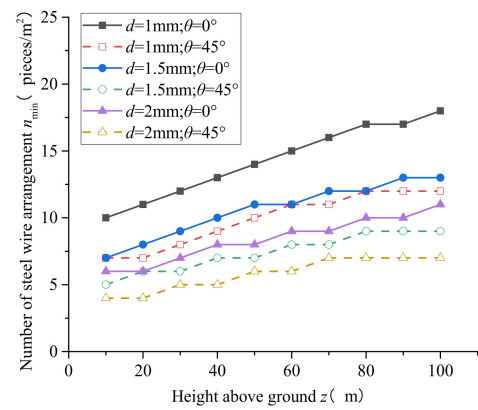
(a)  $L = 30 \text{ mm}$



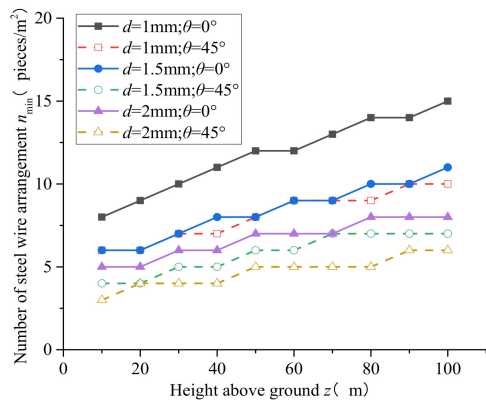
(b)  $L = 40 \text{ mm}$



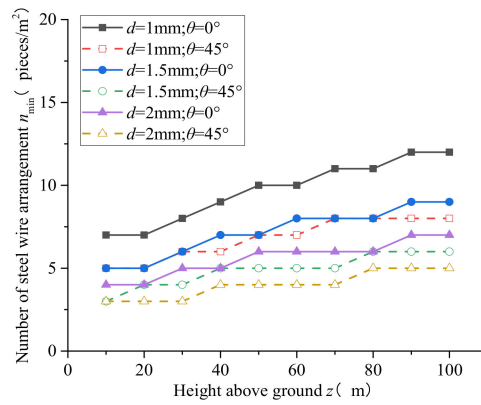
(c)  $L = 50 \text{ mm}$



(d)  $L = 60 \text{ mm}$



(e)  $L = 80 \text{ mm}$



(f)  $L = 100 \text{ mm}$

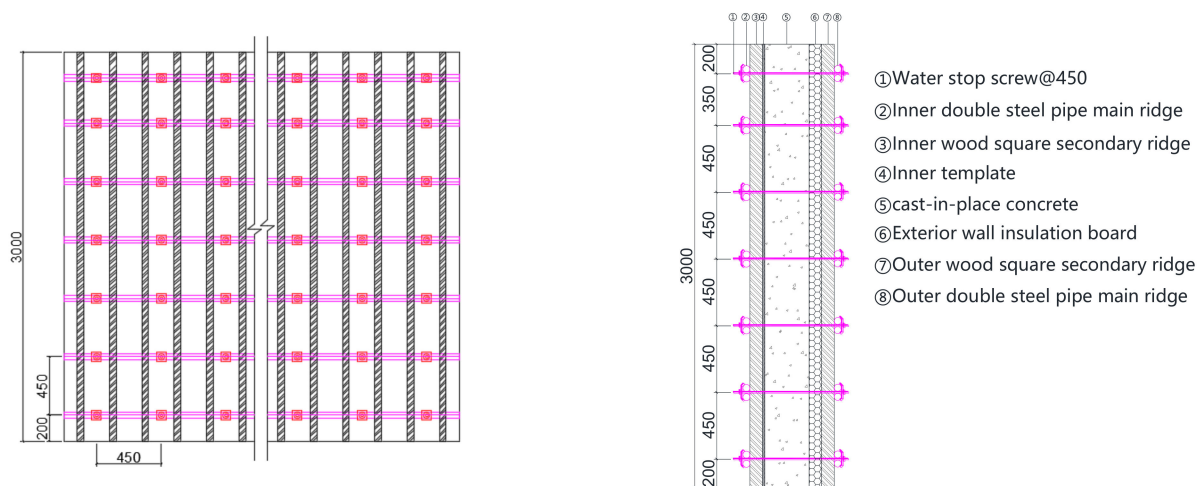
**Figure 9.** Relationship between the height above the ground and the minimum number of steel wires ( $\rho = 2385 \text{ kg/m}^3$ ).

**Table 6.** Number of steel wire layouts per square meter of integrated thermal insulation structure system ( $\theta = 45^\circ$ ).

Height above Ground $z$ (m)	$z < 20$	$20 \leq z < 50$	$50 \leq z \leq 100$
$d = 1 \text{ mm}; L = 30 \text{ mm}$	$\geq 22$	$\geq 30$	$\geq 38$
$d = 1.5 \text{ mm}; L = 30 \text{ mm}$	$\geq 18$	$\geq 24$	$\geq 30$
$d = 2 \text{ mm}; L = 30 \text{ mm}$	$\geq 14$	$\geq 20$	$\geq 24$
$d = 1 \text{ mm}; L = 40 \text{ mm}$	$\geq 20$	$\geq 26$	$\geq 32$
$d = 1.5 \text{ mm}; L = 40 \text{ mm}$	$\geq 14$	$\geq 20$	$\geq 24$
$d = 2 \text{ mm}; L = 40 \text{ mm}$	$\geq 12$	$\geq 16$	$\geq 20$
$d = 1 \text{ mm}; L = 50 \text{ mm}$	$\geq 16$	$\geq 22$	$\geq 28$
$d = 1.5 \text{ mm}; L = 50 \text{ mm}$	$\geq 12$	$\geq 16$	$\geq 22$
$d = 2 \text{ mm}; L = 50 \text{ mm}$	$\geq 10$	$\geq 14$	$\geq 16$
$d = 1 \text{ mm}; L = 60 \text{ mm}$	$\geq 14$	$\geq 20$	$\geq 24$
$d = 1.5 \text{ mm}; L = 60 \text{ mm}$	$\geq 12$	$\geq 14$	$\geq 18$
$d = 2 \text{ mm}; L = 60 \text{ mm}$	$\geq 8$	$\geq 12$	$\geq 14$
$d = 1 \text{ mm}; L = 80 \text{ mm}$	$\geq 12$	$\geq 16$	$\geq 20$
$d = 1.5 \text{ mm}; L = 80 \text{ mm}$	$\geq 8$	$\geq 12$	$\geq 14$
$d = 2 \text{ mm}; L = 80 \text{ mm}$	$\geq 8$	$\geq 10$	$\geq 12$
$d = 1 \text{ mm}; L = 100 \text{ mm}$	$\geq 10$	$\geq 14$	$\geq 16$
$d = 1.5 \text{ mm}; L = 100 \text{ mm}$	$\geq 8$	$\geq 10$	$\geq 12$
$d = 2 \text{ mm}; L = 100 \text{ mm}$	$\geq 6$	$\geq 8$	$\geq 10$

#### 4. Stress Analysis of Integrated Formwork of External Wall Thermal Insulation Structure

Combined with the actual engineering application (as shown in Figure 10), the inner side of the outer wall is made of 15 mm thick wood plywood, the outer side is made of the composite thermal insulation board, and the second ridge is made of 35 mm  $\times$  85 mm square timber, using double steel pipes for the main ridge. The split water stop screw is used for reinforcement, and the screw is arranged horizontally and longitudinally with equal spacing.

**Figure 10.** Schematic diagram of integrated formwork of external wall thermal insulation structure.

The formwork directly bears the load transmitted by the wall. In this paper, the load transmitted by the wall is considered a uniformly distributed load, and the three-span continuous beam is used for the stress analysis of the formwork, as shown in Figure 11.

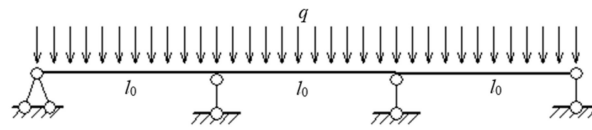


Figure 11. Calculation diagram of a three-span continuous beam.

$$W = \frac{b_0 h_0^2}{6} \quad (9)$$

$$I = \frac{b_0 h_0^3}{12} \quad (10)$$

$$M_{\max} = \frac{q l_0^2}{10} \quad (11)$$

$$\sigma = \frac{M_{\max}}{W} \leq [\sigma] \quad (12)$$

$$\omega_{\max} = \frac{5 q_0 l_0^4}{384 E I} < [\omega] \quad (13)$$

In the above equations,  $W$  is the section resistance moment;  $I$  is the section moment of inertia;  $b_0$  is the calculated width of the template;  $h_0$  is the thickness of formwork;  $M_{\max}$  is the maximum calculated bending moment;  $q$  is the lateral pressure load combination of the formwork,  $q_0$  is the lateral pressure line load acting on the formwork,  $q_0 = 10q/1000$ ;  $l_0$  is the spacing between timbers;  $\sigma$  is bending strength;  $[\sigma]$  is the allowable bending strength;  $\omega_{\max}$  is the maximum calculated deflection;  $[\omega]$  is the allowable deflection. The values of relevant parameters are shown in Table 7.

Table 7. Values of relevant material parameters.

Factor	Variable	
	Plywood	Thermal Insulation Board
Calculated width of template $b_0$ (mm)		1000
Spacing of wood square $l_0$ (mm)		150; 200
Formwork thickness $h_0$ (mm)	15	50; 80; 100
Modulus of elasticity of formwork $E_0$ (N/mm <sup>2</sup> )	4000	20
Allowable bending strength of formwork $[\sigma]$ (N/mm <sup>2</sup> )	15	10
Allowable deflection of formwork $[\omega]$ (mm)		10/250

The mechanical properties of composite thermal insulation board and common plywood are compared. The bending strength  $\sigma$  and deflection  $\omega$  are analyzed, respectively. The corresponding calculation results are shown in Figures 12 and 13. It can be seen from Figure 12 that under the condition of the same spacing of wood square, the bending strength produced by the composite thermal insulation board is far less than that of the plywood. The main reason is that the insulation board has a particular strength, and its thickness is far greater than that of plywood, so the bending resistance of the former is better than that of the latter. Figure 13 compares the deflection deformation of two types of formwork under uniformly distributed load  $q$ . The results showed that the anti-deformation effect of the composite thermal insulation board with a thickness of  $h_0 \geq 80$  mm was close to that of the ordinary plywood under the condition of the same spacing of wood square. In addition, when the spacing of wood square is  $l_0 = 200$  mm, the uniformly distributed load  $q \leq 40$  kN/m that the 50 mm thick thermal insulation board can bear, and the corresponding cast-in-place wall thickness  $h \leq 300$  mm, can also meet the construction requirements of external wall formwork.

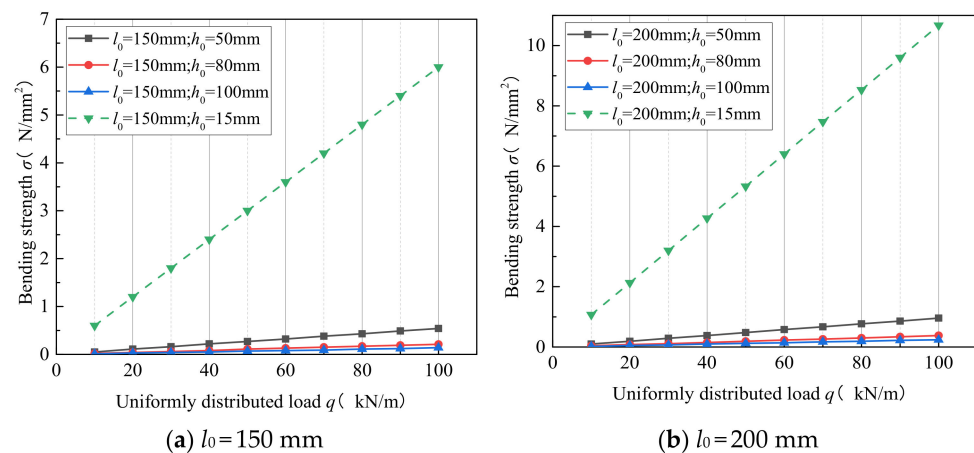


Figure 12. Comparison of bending strength of different formworks.

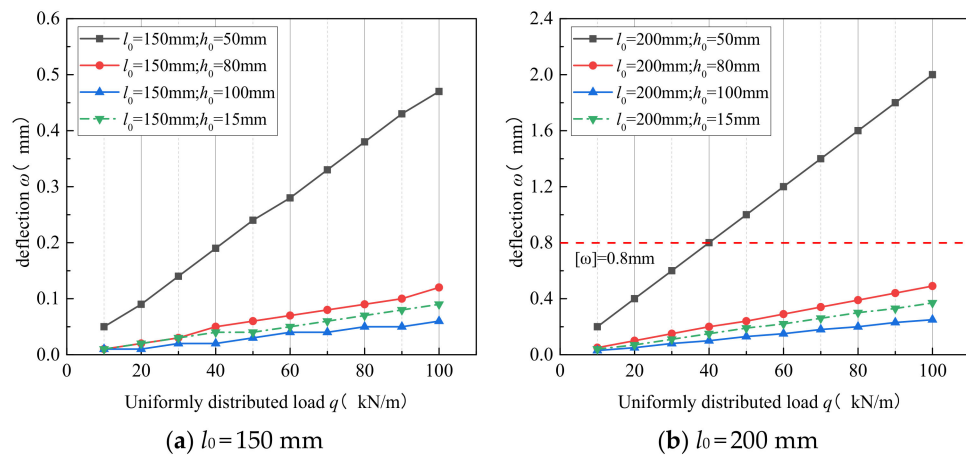


Figure 13. Deflection comparison of different formworks.

In sum, according to the analysis of the bending strength and deflection of the formwork, it is found that the composite thermal insulation board can be used as the formwork instead of plywood so as to achieve the integration of thermal insulation and structure of the building structure. It can be useful for avoiding formwork removal while ensuring the external wall's energy conservation and thermal insulation. It is worth noting that in the actual project, when the thickness of the thermal insulation board used in some parts is less than 50 mm, it is recommended that the spacing of timbers should not exceed 150 mm in order to ensure that the external wall is free from formwork removal, and the stability of the thermal insulation board formwork system.

## 5. Conclusions

This paper establishes a theoretical model of wire pull-out resistance, considering the relationship between wire diameter, wire embedment depth, density of base concrete, steel wire embedment deflection angle, and steel wire pull-out resistance. To do so, the rationality of the theoretical model is verified with relevant test data. Then, based on the advantages of the silicone graphene composite thermal insulation board, the active embedded steel wire knot form in the silicone graphene composite thermal insulation structure integrated system was designed. Based on the theory of wind pressure resistance strength of exterior walls of building structures, taking Shanghai as an example, this paper analyzes the arrangement and quantity of embedded steel wires of composite thermal insulation boards under different building heights. Finally, the comparison and analysis of silicone graphene composite thermal insulation board and ordinary plywood are carried

out from the point of view of external wall formwork stress and deflection. Based on this study, the following conclusions can be drawn:

- (1) By adding the tie steel wires in the silicone graphene composite thermal insulation board, the passive anchoring is changed to an active tie. Through the steel tie wires, the bonding strength between the thermal insulation layer and the concrete base can be actively enhanced, full adhesion without cavities can be guaranteed, and the cost of auxiliary materials and construction procedures can be reduced.
- (2) Based on the pull-out model of steel wire, it is found that the pull-out performance of steel wire is affected by the diameter  $d$  of steel wire, the embedded depth  $L$  of steel wire, and the embedded deflection angle  $\theta$  of steel wire. The impact is significant, and the pull-out resistance is proportional to the three factors. However, when the concrete density (i.e., strength) reaches  $2385 \text{ kg/m}^3$  (C30) and above, it has little effect on the pull-out performance of steel wire.
- (3) Based on the wind pressure resistance strength theory of the external wall of the structure, it is found that the number of steel wires arrangement is inversely proportional to the wire diameter  $d$ , the embedded depth of the steel wire  $L$ , and the embedded deflection angle of the steel wire  $\theta$ . Moreover, the number of steel wires to be arranged increases with the increase of the building height.
- (4) The number of embedded steel wires in the silicone graphene composite thermal insulation board per unit area depends on the building structure's external wall load and the steel wires' pull-out performance. The arrangement of the steel wire determines the bonding performance of the thermal insulation board. When the overall bonding strength meets the wind pressure resistance requirements, the minimum number of steel wires corresponding to different building heights can be obtained.
- (5) When the thickness of the silicone graphene composite thermal insulation board is at least 80 mm, the anti-deformation effect is close to that of the ordinary plywood. The silicone graphene composite thermal insulation board can replace the traditional plywood in the exterior wall formwork system, which can ensure the energy conservation and thermal insulation of the exterior wall and integrate the thermal insulation structure of the building exterior wall, so as to avoid formwork removal.

In this paper, it was proposed to replace the traditional plywood in the exterior wall formwork system with the silicone graphene composite thermal insulation board, and the active embedded steel wire knot form in the silicone graphene composite thermal insulation structure integrated system was designed, realizing the preliminary application of the silicone graphene composite thermal insulation structure integrated system in the project. However, the extensive application of the system in the project requires a more systematic design method and a more standardized construction process flow. There is no doubt that the research work in relevant aspects has a very important engineering application prospect.

**Author Contributions:** Conceptualization, X.Z. and D.G.; methodology, D.G.; software, Z.C.; validation, Z.B., D.G., Q.L. and W.Y.; investigation, Z.B., Y.C.; resources, M.L.; writing—original draft preparation, X.Z.; writing—review and editing, D.G.; visualization, X.Z.; supervision, Z.B.; project administration, M.L. All authors have read and agreed to the published version of the manuscript.

**Funding:** This work was supported by the Construction and scientific research project of the Zhejiang Provincial Department of Housing and Urban-Rural Development (No. 2021K126); the Scientific research project of China Construction 4th Engineering Bureau (No. CSCEC4B-2022-KTA-10, No. CSCEC4B-2023-KTA-10); and Scientific Research Plan of Shanghai Municipal Transportation Commission (No. JT2022-KY-020). The financial support is greatly appreciated.

**Data Availability Statement:** Some or all data that support the findings of this study are available from the corresponding author upon reasonable request.

**Conflicts of Interest:** The authors declare no conflict of interest.

## Abbreviations

The abbreviations, designations and symbols used in the work are as follows:

$f$	the interfacial bond strength between steel wire and concrete matrix
$\delta$	the pull-out displacement of steel wire
$f_0$	the peak bond strength at the debonding stage
$\delta_0$	the corresponding pull-out displacement at the end of the debonding stage
$L$	the embedded depth of steel wire
$d$	the diameter of steel wire
$F_0$	the elastic bonding force between steel wire and concrete matrix
$F_{\max}$	the maximum pull-out resistance of steel wire
$\theta$	the embedded deflection angle of steel wire
$\varepsilon$	the deflection angle influence coefficient
$\rho$	the concrete density
$R_K$	the wind pressure resistance strength
$W_K$	the standard value of wind load
$K$	the wind load resistance safety factor
$F_{\max}$	the maximum pull-out force of the steel wire
$n$	the number of steel wires per square meter
$\eta$	the reduction factor
$z$	the height above ground
$\beta_z$	the gust coefficient at height $z$
$\mu_s$	the local shape coefficient of wind load
$\mu_z$	the wind pressure height variation coefficient
$\omega_0$	the standard value of basic wind pressure
$W$	the section resistance moment
$I$	the section moment of inertia
$b_0$	the calculated width of the template
$h_0$	the thickness of formwork
$M_{\max}$	the maximum calculated bending moment
$q$	the lateral pressure load combination of the formwork
$q_0$	the lateral pressure line load acting on the formwork
$l_0$	the spacing between timbers
$\sigma$	the bending strength
$[\sigma]$	the allowable bending strength
$\omega_{\max}$	the maximum calculated deflection
$[\omega]$	the allowable deflection
$E_0$	the modulus of elasticity of formwork

## References

1. Aksakal, B.; Ulutaş, A.; Balo, F.; Karabasevic, D. A new hybrid MCDM model for insulation material evaluation for healthier environment. *Buildings* **2022**, *12*, 655. [\[CrossRef\]](#)
2. Dénes, T.O.; Iştoan, R.; Tămaş-Gavrea, D.R.; Manea, D.L.; Hegyi, A.; Popa, F.; Vasile, O. Analysis of sheep wool-based composites for building insulation. *Polymers* **2022**, *14*, 2109. [\[CrossRef\]](#) [\[PubMed\]](#)
3. Rasmussen, F.N.; Andersen, C.E.; Wittchen, A.; Hansen, R.N.; Birgisdóttir, H. Environmental product declarations of structural wood: A review of impacts and potential pitfalls for practice. *Buildings* **2021**, *11*, 362. [\[CrossRef\]](#)
4. Barrigón Morillas, J.M.; Montes González, D.; Vílchez-Gómez, R.; Gómez Escobar, V.; Maderuelo-Sanz, R.; Rey Gozalo, G.; Atanasio Moraga, P. Virgin natural cork characterization as a sustainable material for use in acoustic solutions. *Sustainability* **2021**, *13*, 4976. [\[CrossRef\]](#)
5. Li, T.T.; Chuang, Y.C.; Huang, C.H.; Lou, C.W.; Lin, J.H. Applying vermiculite and perlite fillers to sound-absorbing/thermal-insulating resilient PU foam composites. *Fibers Polym.* **2015**, *16*, 691–698. [\[CrossRef\]](#)
6. König, J.; Nemanič, V.; Žumer, M.; Petersen, R.R.; Østergaard, M.B.; Yue, Y.; Suvorov, D. Evaluation of the contributions to the effective thermal conductivity of an open-porous-type foamed glass. *Constr. Build. Mater.* **2019**, *214*, 337–343. [\[CrossRef\]](#)
7. Fernandes, F.A.D.S.; Costa, D.D.S.d.O.; Martin, C.A.G.; Rossignolo, J.A. Vitreous Foam with Thermal Insulating Property Produced with the Addition of Waste Glass Powder and Rice Husk Ash. *Sustainability* **2023**, *15*, 796. [\[CrossRef\]](#)
8. Ahac, M.; Ahac, S.; Lakušić, S. Long-Term Sustainability Approach in Road Traffic Noise Wall Design. *Sustainability* **2021**, *13*, 536. [\[CrossRef\]](#)
9. Pedroso, M.; Flores-Colen, I.; Silvestre, J.D.; Gomes, M.G.; Silva, L.; Ilharco, L. Physical, mechanical, and microstructural characterisation of an innovative thermal insulating render incorporating silica aerogel. *Energy Build.* **2020**, *211*, 109793. [\[CrossRef\]](#)

10. Paneri, A.; Wong, I.L.; Burek, S. Transparent insulation materials: An overview on past, present and future developments. *Sol. Energy* **2019**, *184*, 59–83. [[CrossRef](#)]
11. Gonçalves, M.; Simões, N.; Serra, C.; Flores-Colen, I. A review of the challenges posed by the use of vacuum panels in external insulation finishing systems. *Appl. Energy* **2020**, *257*, 114028. [[CrossRef](#)]
12. Berardi, U.; Sprengard, C. An overview of and introduction to current researches on super insulating materials for high-performance buildings. *Energy Build.* **2020**, *214*, 109890. [[CrossRef](#)]
13. De Guinoa, A.S.; Zambrana-Vasquez, D.; Alcalde, A.; Corradini, M.; Zabalza-Bribián, I. Environmental assessment of a nano-technological aerogel-based panel for building insulation. *J. Clean. Prod.* **2017**, *161*, 1404–1415. [[CrossRef](#)]
14. Su, S.; Cébron, D.; Nataf, H.C.; Cardin, P.; Vidal, J.; Solazzo, M.; Do, Y. Acoustic spectra of a gas-filled rotating spheroid. *Eur. J. Mech. B Fluids* **2020**, *84*, 302–310. [[CrossRef](#)]
15. Uvsløkk, S.; Schlemminger, C.; Asphaug, S. Thermal insulation performance of reflective foils in floor cavities—Hot box measurements and calculations. *Energy Procedia* **2017**, *132*, 333–338. [[CrossRef](#)]
16. Fei, P.; Guo, Z.; Ye, C.; Teng, Z.; Chen, Q.; Zhang, G.; Cai, J. The enhancement of the flame retardance of bamboo fibre/HDPE composites: Cerium doped H<sub>2</sub>Ti<sub>2</sub>O<sub>5</sub>•H<sub>2</sub>O nanotubes effects. *Constr. Build. Mater.* **2019**, *201*, 728–735. [[CrossRef](#)]
17. Hossain, A.; Mourshed, M. Retrofitting Buildings: Embodied & Operational Energy Use in English Housing Stock. *Proceedings* **2018**, *2*, 1135.
18. Buratti, C.; Belloni, E.; Lascaro, E.; Merli, F.; Ricciardi, P. Rice husk panels for building applications: Thermal, acoustic and environmental characterization and comparison with other innovative recycled waste materials. *Constr. Build. Mater.* **2018**, *171*, 338–349. [[CrossRef](#)]
19. Danihelová, A.; Němec, M.; Gergel, T.; Gejdoš, M.; Gordanová, J.; Ščensný, P. Usage of recycled technical textiles as thermal insulation and an acoustic absorber. *Sustainability* **2019**, *11*, 2968. [[CrossRef](#)]
20. Raza, M.; Abdallah, H.A.; Abdullah, A.; Abu-Jdayil, B. Date Palm Surface Fibers for Green Thermal Insulation. *Buildings* **2022**, *12*, 866. [[CrossRef](#)]
21. Yang, W.; Li, Y. Sound absorption performance of natural fibers and their composites. *Sci. China Technol. Sci.* **2012**, *55*, 2278–2283. [[CrossRef](#)]
22. Abu-Jdayil, B.; Mourad, A.H.; Hittini, W.; Hassan, M.; Hameedi, S. Traditional, state-of-the-art and renewable thermal building insulation materials: An overview. *Constr. Build. Mater.* **2019**, *214*, 709–735. [[CrossRef](#)]
23. Villasmil, W.; Fischer, L.J.; Worlitschek, J. A review and evaluation of thermal insulation materials and methods for thermal energy storage systems. *Renew. Sustain. Energy Rev.* **2019**, *103*, 71–84. [[CrossRef](#)]
24. Asdrubali, F.; D’Alessandro, F.; Schiavoni, S. A review of unconventional sustainable building insulation materials. *Sustain. Mater. Technol.* **2015**, *4*, 1–17. [[CrossRef](#)]
25. Berardi, U.; Iannace, G. Acoustic characterization of natural fibers for sound absorption applications. *Build. Environ.* **2015**, *94*, 840–852. [[CrossRef](#)]
26. Al-Homoud, M.S. Performance characteristics and practical applications of common building thermal insulation materials. *Build. Environ.* **2005**, *40*, 353–366. [[CrossRef](#)]
27. Zhao, Z. The Application of Polyurethane Composite Material in the Field of Building Exterior Wall. In Proceedings of the 2015 International Conference on Social Science and Technology Education, Sanya, China, 11–12 April 2015; Atlantis Press: Amsterdam, The Netherlands, 2015.
28. Li, Z.; Liu, W.; Liu, Y. Experimental Study on Seismic Behavior of Composite Shear Wall with Vitriified Beads No-demolition Wall Formwork. *Concrete* **2012**, *271*, 131–137. (In Chinese)
29. Li, X.; Liu, J.; Pei, X.; Bai, Y. Design and performance analysis of rock wool composite thermal insulation formwork. *Silic. Bull.* **2019**, *38*, 1597–1603. (In Chinese)
30. Qaderi, S.; Ebrahimi, F.; Mahesh, V. Free vibration analysis of graphene platelets–reinforced composites plates in thermal environment based on higher-order shear deformation plate theory. *Int. J. Aeronaut. Space Sci.* **2019**, *20*, 902–912. [[CrossRef](#)]
31. Qaderi, S.; Ebrahimi, F.; Seyfi, A. An investigation of the vibration of multi-layer composite beams reinforced by graphene platelets resting on two parameter viscoelastic foundation. *SN Appl. Sci.* **2019**, *1*, 399. [[CrossRef](#)]
32. Ebrahimi, F.; Qaderi, S. Stability analysis of embedded graphene platelets reinforced composite plates in thermal environment. *Eur. Phys. J. Plus* **2019**, *134*, 349. [[CrossRef](#)]
33. Liu, D.; Wang, S.; Zhu, J.; Li, H.; Zhu, H. Investigation on thermal conductivity of graphene/Si heterostructure based on molecular dynamics simulation. *Phys. Lett. A* **2022**, *426*, 127895. [[CrossRef](#)]
34. Gong, W.; Garg, R.; Guo, R.; Lee, S.; Cohen-Karni, T.; Shen, S. Thermal Transport in Multidimensional Silicon-Graphene Hybrid Nanostructures. *ACS Appl. Mater. Interfaces* **2021**, *13*, 50206–50212. [[CrossRef](#)]
35. Wang, J.; Zhang, J.; Yu, L.; Fu, Y. Experiment and Simulation of Pullout Behavior of Bonded Steel Wire and Concrete. *Eng. Mech.* **2016**, *33*, 202–208. (In Chinese)
36. Zhang, J.; Gao, Y.; Huang, Z. Comparative analysis of temperature and stress of internal and external thermal insulation walls. *J. Harbin Eng. Univ.* **2011**, *32*, 895–905. (In Chinese)
37. Lin, Z.; Kanda, T.; Li, V.C. On interface property characterization and performance of fiber reinforced cementitious composites. *Concr. Sci. Eng.* **1999**, *1*, 173–174.

38. Li, V.C.; Stang, H.; Krenchel, H. Micromechanics of crack bridging in fibre-reinforced concrete. *Mater. Struct.* **1993**, *26*, 486–494. [[CrossRef](#)]
39. Yu, L.; Fu, Y.; Zhang, J.; Wang, J. Experiment and simulation of bond performance between foam concrete and steel wire. *J. Harbin Inst. Technol.* **2016**, *48*, 119–123. (In Chinese)
40. *JGJT480-2019*; Technical Standard for External Thermal Insulation Engineering of Rock Wool Thin Plastered Exterior Walls. Ministry of Construction of the People’s Republic of China: Beijing, China, 2019. (In Chinese)
41. *GB50009-2012*; Code for Building Structure Loads. Ministry of Construction of the People’s Republic of China: Beijing, China, 2012. (In Chinese)
42. *GB/T 5486-2008*; Test Methods for Inorganic Rigid Thermal Insulation. China Standards Press: Beijing, China, 2008. (In Chinese)
43. *JGJ 144-2019*; Technical Standard for External Thermal Insulation on Walls. China Construction Industry Press: Beijing, China, 2019. (In Chinese)
44. *GB/T 10294-2008*; Thermal Insulation—Determination of Steady-State Thermal Resistance and Related Properties-Guarded Hot Plate Apparatus. China Standards Press: Beijing, China, 2008. (In Chinese)
45. *GB/T 19631-2005*; Glassfiber Reinforced Cement Lightweight Hollow Panel for Partition. China Standards Press: Beijing, China, 2005. (In Chinese)
46. *GB/T 8813-2008*; Rigid Cellular Plastics-Determination of Compression Properties. China Standards Press: Beijing, China, 2008. (In Chinese)
47. *GB 8624-2012*; Classification for Burning Behavior of Building Materials and Products. China Standards Press: Beijing, China, 2012. (In Chinese)

**Disclaimer/Publisher’s Note:** The statements, opinions and data contained in all publications are solely those of the individual author(s) and contributor(s) and not of MDPI and/or the editor(s). MDPI and/or the editor(s) disclaim responsibility for any injury to people or property resulting from any ideas, methods, instructions or products referred to in the content.